Advanced Fiber Materials
https://doi.org/10.1007/s42765-024-00430-8

RESEARCH ARTICLE

A Trimode Self-Cleaning Composite Membrane with an Eco-friendly Substrate for Energy-Saving Wastewater Recycling

Yuelin Yu[1] · Yongtao Yu[1] · Hongyi Wu[1] · Jian Shi[1,3] · Hideaki Morikawa[1,2,3] · Chunhong Zhu[1,2,3]

Received: 23 January 2024 / Accepted: 4 May 2024

Abstract

A separation membrane with low or clean energy costs is urgently required for energy-saving and long-term service since electric energy generated from burning non-renewable resources will gradually cause a burden to the environment. At present, the conventional membrane being used in one mode is critical for a variety of scenarios in real life, which suffers from a trade-off effect, short service life, being difficult to recycle after damage. Herein, we report a trimode purification membrane composed of an eco-friendly polycaprolactone (PCL) substrate and functional graphene dioxide/polyaniline (GO/PANI) particles. Due to the photothermal transfer and photocatalytic properties of GO/PANI blend, the composite membrane can absorb 97.44% solar energy to handle natural seawater or mixed wastewater, which achieves a high evaporation rate of 1.47 kg m^{-2} h^{-1} in solar-driven evaporation mode. For the photocatalytic adsorption–degradation mode, 93.22% of organic dyes can be adsorbed and degraded after 12 h irradiation under 1 kW m^{-2}. Moreover, electric-driven cross-flow filtration mode as a supplement also shows effective rejection over 99% for organic dyes with a high flux over 40 L m^{-2} h^{-1} bar^{-1}. The combination of solar-driven evaporation, photocatalytic adsorption–degradation, and electric-driven cross-flow filtration demonstrates a prospective and sustainable strategy to generating clean water from sewages.

Keywords Trimode purification · Eco-friendly substrate · Self-cleaning and anti-fouling · Energy-saving · Seawater desalination

1 Introduction

Although 71% of our planet is covered by all kinds of water, only a small part of it can be directly used as freshwater due to the high salt content of seawater (97%), the limited accessibility of glaciers, ground water, and others [1, 2]. Nevertheless, even this little part has been greatly polluted by the rapidly growing population, industry development, and natural disasters [3, 4]. According to the Sustainable Development Goals (SDGs) report of the United Nations (UN), during 2015 and 2022, about 2.2, 3.5, and 2.0 billion population cannot achieve safely managed drinking water, sanitation, and basic hygiene services, respectively (SDG 6: clean water and sanitation) [5].

As an effective solution to the severe water scarcity problem, the membrane separation technology has been widely used for the recycling of wastewater. The separation membrane can be fabricated by non-solvent induced phase conversion [6, 7], interfacial polymerization (IP) [8, 9], vacuum filtration [10, 11] electrospinning [12, 13], etc. Of note, the electrospinning nanofibrous membrane shows great potential for water purification originated from its high porosity, tunable pore size, and large specific surface area [14, 15]. However, synthetic polymers, such as polyacrylonitrile (PAN) [15], poly(vinylidene fluoride) (PVDF) [16], polyethyleneimine (PEI) [15, 17], and polyimide (PI) [17, 18], are highly used for electrospinning due to their easy processability and thermal stability. Most of them are non-degradable and cause a great burden to the environment when they are scrapped after long-term service [19]. Herein, degradable materials have great potential for the sustainable

✉ Chunhong Zhu
zhu@shinshu-u.ac.jp

[1] Graduate School of Medicine, Science and Technology, Shinshu University, 3-15-1, Tokida, Ueda, Nagano 386-8567, Japan

[2] Institute for Fiber Engineering (IFES), Interdisciplinary Cluster for Cutting Edge Research (ICCER), Shinshu University, 3-15-1, Tokida, Ueda, Nagano 386-8567, Japan

[3] Faculty of Textile Science and Technology, Shinshu University, 3-15-1, Tokida, Ueda, Nagano 386-8567, Japan

Published online: 22 May 2024

development. PCL as one of the biodegradable polymers can be highlighted, which is a semi-crystalline aliphatic polyester and the ester bond can be hydrolyzed to form acid monomers. The nontoxic and flexible properties of PCL make it a suitable candidate for electrospinning materials. Moreover, it degrades relatively slowly due to its high crystallinity and low hydrolysis rate, and after combine with other materials it can be applied for long-term water purification [20, 21].

As for the membrane separation methods, most of them, such as dead-end filtration, cross-flow filtration, and electrodialysis, require extra electric energy to provide pressure or electricity difference, which increase the environmental risk since electric power is still mainly generated from coal burning and fossil fuels. Therefore, a solar-driven interfacial evaporation method based on photothermal phenomenon emerges and is urgently hoped to be an alternative way since solar energy is clean, safe, and sustainable [22, 23]. Moreover, light will be reflected continuously in the pores and nanofibers of the electrospinning membrane, making full use of diffuse reflection and enhancing light absorption [24]. Thus, the combination of electrospinning technology and solar-driven interfacial evaporation technology shows great potential in the water purification field. Nevertheless, the evaporation rate of solar-driven evaporation membranes (usually below 3 kg m^{-2} h^{-1} sun^{-1}) is generally smaller than the flux of traditional filtration membranes (such as nanofiltration, which usually exceeds 10 L m^{-2} h^{-1} bar^{-1}) and the membrane is prone to be contaminated after long-term service, which hinders its application [25–27]. Therefore, a multi-scenario applicable membrane with self-cleaning property that can be used in multi-mode is urgently needed for the diversity demands in real life.

The solar-driven interfacial evaporation process is realized utilizing photothermal conversion materials, such as metals and metal compounds [28], carbon materials (carbon black, graphene, carbon nanotubes, MXene, etc.) [29, 30], polymers (polydopamine, polypyrrole, polyaniline, etc.) [31–34], and others. Of them, conductive PANI attracted widespread interests owing to its merits of excellent environment stability, low cost, and convenient production [35]. Most importantly, PANI consisting of benzenoid and quinonoid units is a special organic semiconductor photocatalysts, which has a wide range of delocalized π–π conjugated structures in its molecules [36–38]. Thus, photothermal and photocatalyst properties of PANI provide a strategy for multi-functional purification membrane. However, pure PANI is limited by its poor quantum efficiency and mechanical strength, which calls for the combination with other materials. Graphene is an effective choice, which is also a photothermal material that shows excellent performance in mechanical properties, such as extremely high modulus (about 1 TPa), tensile strength (about 100 GPa) [39, 40], thermal stability, and electrical conductivity [41, 42]. It has wide spectra of absorption capacity, which can enhance its ability to convert solar energy into heat to generate vapor [43–46]. Besides, GO can be mixed with polymer solution for electrospinning, therefore embedded within the polymer matrix rather than coating on the surface [47].

In this study, a nanofibrous membrane substrate has been fabricated by electrospinning of PCL/GO and then modified by in situ polymerization process as the huge specific surface area of GO nanoparticles and nanofibers offers numerous sites for the attachment of PANI. Of them, polymer PCL provides the basic skeleton of the membrane, which is biodegradable that will not cause burden to the environment when it becomes invalid after long-term work. Meanwhile, GO and PANI work synergistically as functional materials to obtain better photothermal and photocatalytic properties. After characterizing functionalization, chemical compositions, morphology, wettability, and solar absorption property of membranes, the purification performance and the mechanism were evaluated in detail. It turns out that the fabricated composite membrane can be applied in trimode of solar-driven evaporation, photocatalytic degradation, and cross-flow filtration for recycling wastewater in different circumstances. This work provides a new strategy of purification membrane that is highly efficient, sustainable, and practical for solving the serious water crisis problem or recovering scarce resources from sewage.

2 Experimental Section

2.1 Materials

Polycaprolactone (PCL, $M_w = 80{,}000$) was supplied by BOWENSHUHUA Co., Ltd. (China). Graphene nanoplatelets (6–8 nm thick, 15 μm wide), nitric acid (HNO_3, 69% purity), n-dimethylformamide (DMF, 99.5% purity), acetone (99.5% purity), phytic acid (50% purity), aniline (99% purity), ammonium persulfate (APS, 98% purity), Methyl Orange (MO, $C_{14}H_{14}N_3SO_3Na$), and ethanol (EtOH) were all provided by FUJIFILM Wako Pure Chemical Co., Ltd. (Japan). The deionized (DI) water was supplied by WG250B, Yamato Scientific Co., Ltd. (Japan).

2.2 Synthesis of Graphene Dioxide

GO was obtained by functionalizing pristine graphene for further use. In detail, 1 g graphene was mixed with 100 mL 3 mol/L HNO_3 solution and stirred at 120 °C for 8 h. After cooling to room temperature, the mixture was filtered and washed by deionized water through Buchner funnel connected with a vacuum pump. The synthesized GO was dried in oven for 12 h at 50 °C and then grinded homogeneously before use.

2.3 Preparation of Nanofibrous Membrane

For the preparation of nanofiber-support layer, PCL pellets were dissolved in DMF/Acetone (7:3 by volume) solvent mixture by stirring at 60 °C for 12 h to obtain 16 wt% aqueous solution. Afterward, the fibrous membranes were fabricated by an electrospinning machine assembled by our lab. The spinning solutions were loaded to a plastic syringe (5 mL) equipped with a 21 G stainless steel needle (outer diameter = 0.80 mm). The electrospinning process was performed under the following parameters: 9.5 kV voltage, 1 mL/h feed rate, 20 cm distance from needle tip to the collector which was covered by aluminum foil. During the spinning process, temperature and relative humidity (RH) were controlled at 25 ± 5 °C and 35 ± 5%, respectively. Then, the concentration of PCL was stabled at 16 wt%, several PCL/GO composite spinning solutions were prepared with a gradient mass ratio of GO (1, 3, 5, and 7 wt%) with respect to the PCL content, which were named PG1, PG3, PG5, and PG7. And PG means all the PCL/GO nanofibrous membranes, P16 means the pure PCL membrane.

2.4 In Situ Polymerization of Polyaniline

PANI was in situ-polymerized on the surface of PG5 via dip-coating method. First, phytic acid and aniline were added to DI water, stirring for 30 min. The nanofibrous membrane was then dipped in the solution and mixed for 1 h. Meanwhile, APS particles were dissolved in another 20 mL DI water and stirred until completely dissolved. After that, APS solution was gradually added to above-mentioned combined solution within 20 min and then stirred for another 2 h. The polymerized membrane was washed by EtOH and DI water several times to remove superfluous solvent and additives under ultrasonic conditions. The total solution volume is 100 mL, and the concentration ratio of phytic acid, aniline, and APS was fixed at 1:10:10, and the concentration of aniline was varied across several levels: 0.01, 0.03, 0.05, 0.1, and 0.2 mol/L. The fabricated composite membranes were named as PGA1, PGA2, PGA3, PGA4, and PGA5, respectively, while PGA means all the PCL/GO/PANI composite membranes.

2.5 Characterization

The Raman spectroscope (Hololab 5000, ST Japan Inc.) was applied to characterize the graphene before and after functionalization. Chemical composition and functional groups of membranes were analyzed by the X-ray photoelectron spectroscopy (XPS, AXIS-ULTRA HSA SV, Japan) and Fourier-transform infrared spectrophotometer (FTIR-6600, Jasco, Japan). Surface morphology and cross-sectional structure of the prepared membranes were investigated by field emission scanning electron microscopy (FESEM, JSM-IT800SHL, Japan). The wettability of membranes was observed by a contact angle meter (DMs-400, Kyowa Interface Science Co., Ltd., Japan). Optical absorbance, transmission, and reflection of membranes were measured by a ultraviolet–visible–near-infrared spectrophotometer (UV-3600, MPC-3100, Shimadzu Co., Ltd., Japan). The concentrations of salt ions (Na^+, Mg^{2+}, K^+, and Ca^{2+}) were analyzed by an inductively coupled plasma emission spectroscopic analyzer (ICP, SPS3100, Hitachi Co., Ltd., Japan). The dye concentrations were measured by UV–vis spectroscopy (UV-2700, Shimadzu Co., Ltd., Japan).

3 Results and Discussion

3.1 Fabrication and Characterization of PCL/GO/PANI Composite Membrane

As shown in Fig. 1, for trimode recycling of wastewater, graphene was first synthesized into GO for incorporation of hydrophilic chemical groups like –OH and –OOH (Fig. 1a), which could be blended more evenly with PCL and offer more position for hydrogen band (Fig. 1d). GO particles were then mixed with biodegradable polymer PCL uniformly for electrospinning, and then PANI was in situ-polymerized on the base of above nanofibrous membrane (Fig. 1b). Membrane of pure PCL was denoted as P16, PCL/GO membranes were called PG, and PCL/GO/PANI was named as PGA.

Raman spectroscopy was used to evaluate structural integrity and functionalization degree of carbonaceous materials such as GO, which exhibits two characteristic bands: the disorder mode D band (≈ 1350 cm^{-1}) and the tangential stretching mode (vibrations along the tube axis) *G* band (1500–1600 cm^{-1}) [48, 49]. Generally, the *D* band is assigned to sp3 carbon atoms at defect sites, while the *G* band is associated with sp2 carbon atoms, and the I_D: I_G band intensity ratio provides a metric of the overall graphene structure [50, 51]. As shown in Fig. 2a, both pristine graphene and GO exhibit two peaks at 1344 cm^{-1} and 1575 cm^{-1}, which relate to D band and G band. Furthermore, the I_D: I_G ratio of GO (1.00) is obviously higher than the pristine graphene (0.64), which indicates the high functionalization degree of graphene after the surface modification.

XPS was utilized to analysis the surface chemical composition of the nanofibrous membrane, and the survey spectra of three typical membranes (P16, PG5, PGA3) is shown in Fig. 2b. For the P16, two characteristic peaks of C1s around 285 eV and O1s around 530 eV can be detected obviously, while these two peaks still can be found in PG5 and the intensity of O1s is scarcely decreased [52]. It indicates that GO nanoparticles are embedded into PCL polymer evenly and conform nanofibers together but not just stack up on

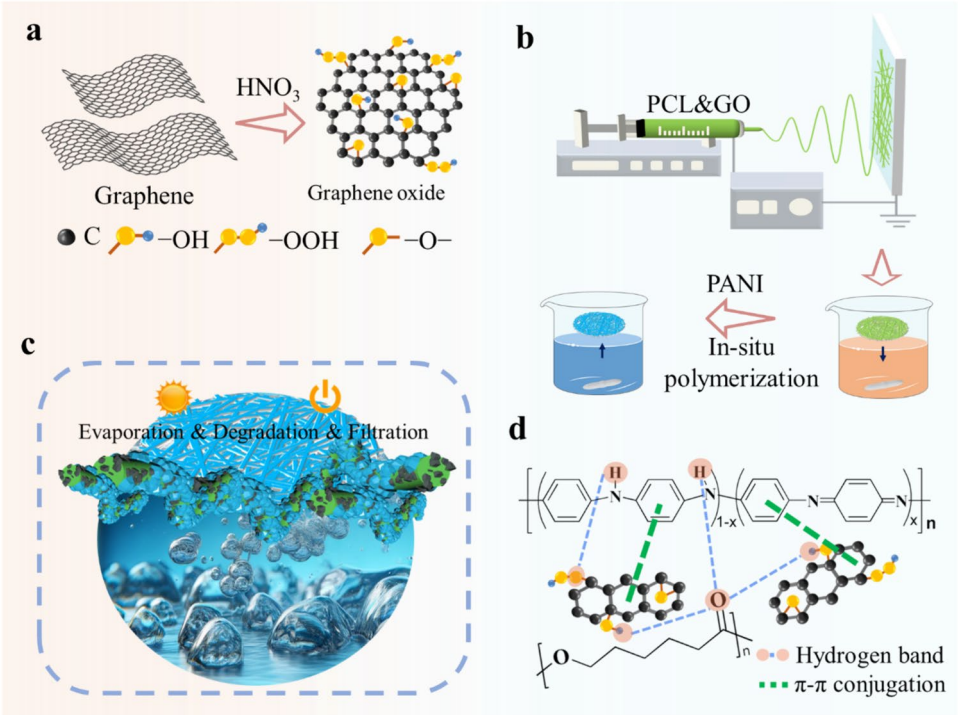

Fig. 1 Schematic illustration of a trimode functional PGA membrane. **a** Synthesis of graphene dioxide. **b** Preparation of nanofibrous membrane and in situ polymerization of PANI. **c** Solar-driven evaporation, adsorption–degradation, and cross-flow filtration trimode recycling of wastewater. **d** Interfacial interactions between PCL, GO, and PANI

the surface of PCL nanofibers, since the intensity of O1s is clearly smaller than the intensity of C1s for pure GO powder (Fig. S1). Three characteristic peaks are exhibited in the survey spectra of PGA3, despite from C1s and O1s same as P16 and PG5, a new peak of N1s around 400 eV appears due to the existence of PANI after in situ polymerization [53, 54].

To further confirm the existence of PANI and structure of each component in the composite membrane, FTIR spectrums were tested and the results are shown in Fig. 2c. For the P16, two strong peaks near 1723 cm^{-1} and 1166 cm^{-1} are due to C=O stretching and C–O stretching of PCL, respectively. Meanwhile, two weaker characteristic peaks around 2948 cm^{-1} and 2856 cm^{-1} correspond to asymmetrical stretch and symmetrical elongation of CH_2, respectively. Besides, the asymmetrical elongation peak of C–O–C appears at 1244 cm^{-1}, and the peak at 1047 cm^{-1} is according to the existence of C–O [52, 55, 56]. Because of the scarce IR activity of carbonaceous materials, P16 and PG5 show similar characteristic peaks since GO is scarcely detectable [57]. After the modification of PANI, two new peaks at 1585 cm^{-1}, 1497 cm^{-1} originated from C = C on the quinone ring mixed with –NH bending vibration, C=N stretching vibration mixed with C–H bending vibration appear, respectively. Notably, a new peak at 3240 cm^{-1} attributed to –OH stretching vibration is found in PGA3 (Fig. S2), which was generated from the strong interactions between GO/PANI (including electrostatic forces, hydrogen bonding, and π–π conjugation as shown in Fig. 1d) and the adoption of phytic acid [58, 59]. Moreover, those six typical peaks of P16 and PG5 still exist, suggesting that the in situ polymerization does not destroy the component integrity of substrate membrane.

Optical observations of P16, PG, and PGA membranes are shown in Fig. S3. From the digital photographs, we can see that the pure PCL membrane (P16) is white and turns to gray (PG) after the introduction of GO, and the gray deepens as the GO mass increases. The color eventually becomes dark green (PGA) after in situ polymerization of PANI, which apparently proves the success of the surface modification. The surface morphologies were further characterized by FESEM. For PG nanofibrous membranes (Fig. 2d1–d5), a typical interconnected pore structure network is observed, and the inset figure shows the distribution of nanofibers diameters. The comparison of average diameter changes is listed in Fig. 2d6. The diameter decreases slightly while adding more GO nanoparticles, but when the content of GO increases to 7 wt%, some agglomeration appears, which is harmful to the structure uniformity (Fig. 2d5). Therefore, the concentration of GO is fixed at 5 wt%, and PANI is decorated on the base of PG5. Different

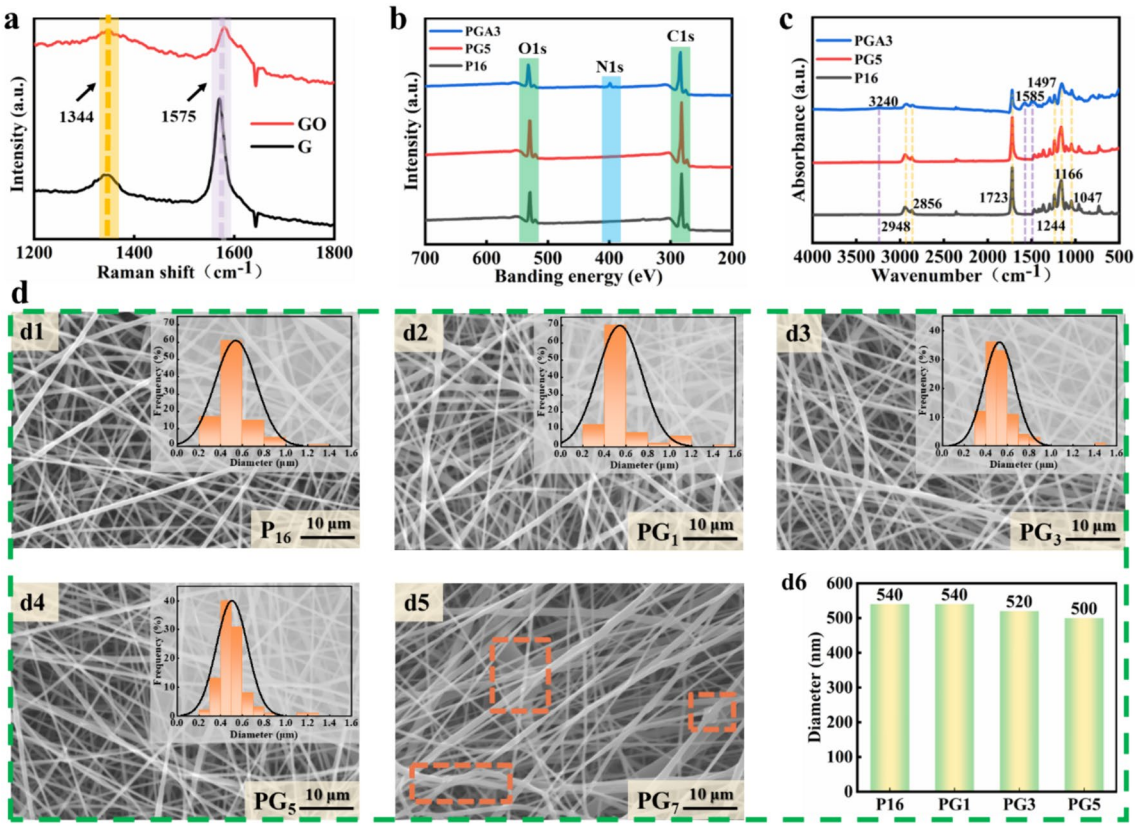

Fig. 2 Characterizations of GO powders and PG membranes. **a** Raman spectrum of graphene before and after modification. **b** Wide XPS spectra and **c** FTIR spectra of P16, PG5, PGA3 membranes. **d** SEM images (**d1–d5**, the inset is diameter distribution) and diameter comparison (**d6**) of P16, PG membranes

magnification images of PGA composite membranes are shown in Fig. 3a–e. Contrary to the smooth surface of PG, PGA membranes turn to be roughness owing to the numerous PANI particles wrapped on the nanofibers. The high specific surface area of nanofibers and GO nanoparticles offers tremendous sites for the attachment of PANI, it visibly grows in number when the concentration of aniline increased from 0.01 to 0.05 mol/L (Fig. 3a–c), and then almost reaches a balance which does not change too much with the concentration growth (Fig. 3c–e). Since the over aggregation of PANI will block the pores of nanofibrous membranes severely thus decline the water flux and light absorption property, PGA3 was therefore adopted for the further analysis. The color and morphology vary once again, verifying the existence of GO and PANI, which are consistent with the Raman, XPS, and FTIR results.

3.2 Solar-Driven Evaporation Performance

Photothermal materials can adsorb solar energy at different wavelengths and turn into thermal energy which can be used to heat wastewater. Liquid water will be transformed into water vapor and harvested as fresh water, while other pollutants particles are difficult to be evaporated and therefore separated from water molecules. Therefore, the ultraviolet–visible–near-infrared (UV–vis–NIR) absorption of membranes with different components were measured to assess the solar-harvesting performance before evaporation test. As shown in Fig. 3f, the absorption of pure PCL membrane (P16) is around 33.52%, which greatly increases to 84.41% (PG5) after incorporating GO, showing a significant enhancement across a wide spectral range of 300–1800 nm. Moreover, the absorption reaches up to 97.44% (PGA3) for the PANI-modified membrane, verifying the essential of GO and PANI in improving the light absorption property and indicating an outstanding photothermal effect. The water contact angle (WCA) was measured for wettability evaluation, and the result is shown in Fig. 3g and Fig. S4 (inset image of P16 and PG5 were taken at 1000 ms, but for PGA3, they were taken at 200 ms since the water was totally adsorbed by PGA3 at 1000 ms). It can be seen that WCA decreases to below 90° after PANI modification, indicating an improvement in wettability, which is beneficial for purification membrane. A more hydrophilic surface generally enhances the speed at which water molecules traverse the

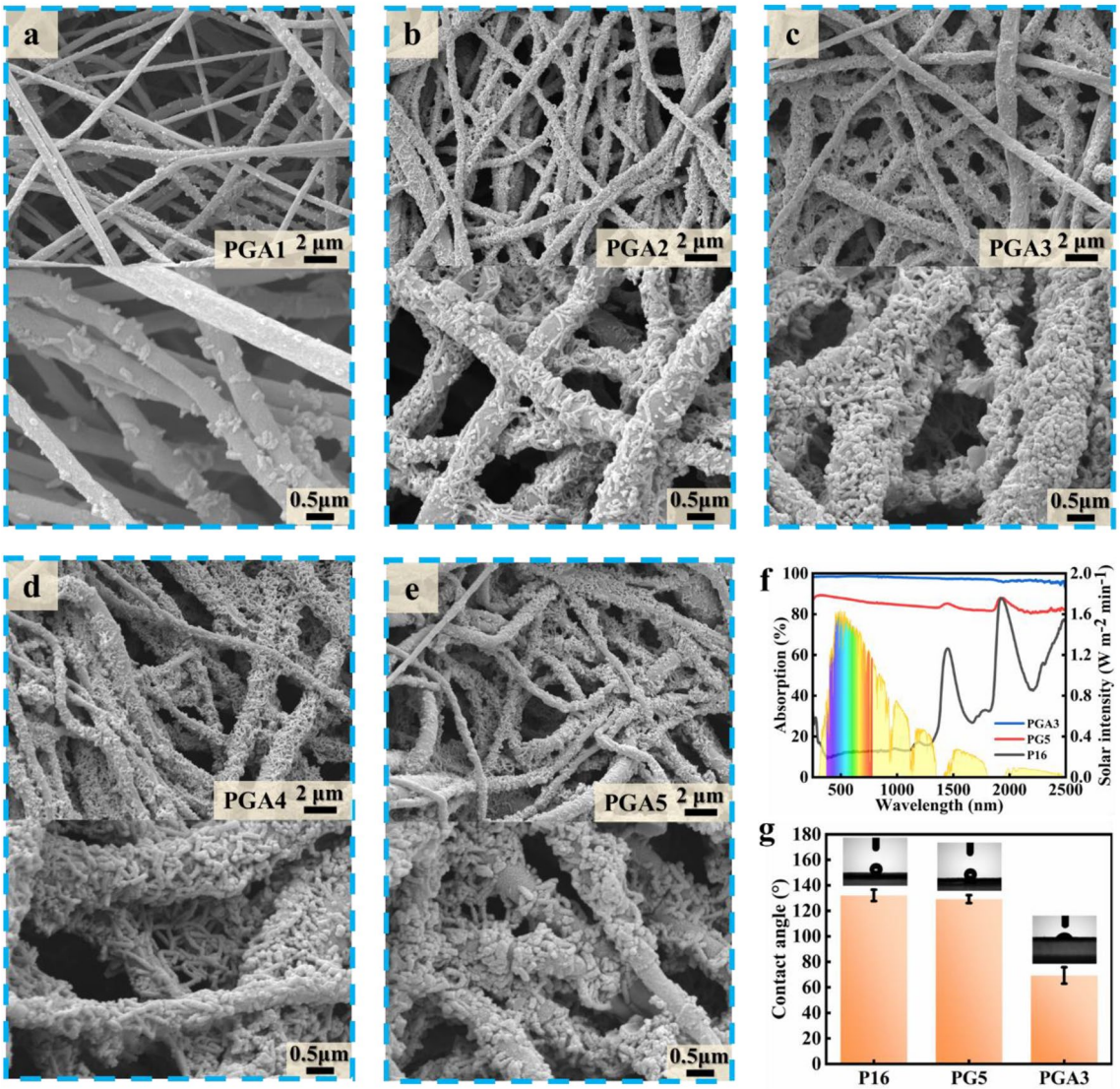

Fig. 3 Morphology and property of membranes. **a–e** FESEM images of PGA membranes with different magnifications. **f** Solar absorption spectra of P16, PG5 and PGA3 (left-hand side axis), and solar spectra irradiance (right hand side axis) under light intensity of 1 kW m^{-2}. **g** Wettability of P16, PG5 (1000 ms), and PGA3 (200 ms)

membrane and reduces fouling by forming a hydration layer between the membrane and the feed solution [60–63].

For purifying wastewater on sunny days by the use of solar energy (Fig. 4a), a simulated evaluation system was self-assembled. As shown in Fig. 4b, a solar simulator (XES-40S3-TT, SAN-EI Electric, Japan) and a custom-made interfacial solar evaporator is adopted the same as our previous study at temperature of 26 ± 2 °C and humidity of 50 ± 5% [25]. The real-time weight loss of water was recorded by an electronic balance (GR-200, A&D company, Limited, Japan) connected to a computer. Besides, the surface temperatures of membranes were monitored by an infrared thermal imaging camera (Testo 875-2 I setV3, German).

On the one hand, the photothermal effect can be evaluated by evaporation rate v through Eq. (1).

$$v = \frac{m_1 - m_2}{A \times \Delta t} \tag{1}$$

where m_1 and m_2 (kg) refer to the weight of evaporator before and after evaporation, respectively. A (m^2) refers to effective evaporation area and Δt (h) refers to evaporation time. As presented in Fig. 4c, the mass change of PGA membranes is significantly higher than that of PG, P16, and other control samples. The evaporation rate for 1 h solar illumination of blank DI water is only 0.44 kg m^{-2} h^{-1}, which increases to 0.67 kg m^{-2} h^{-1} after adding cotton wick due to capillary effect (Fig. 4d). However, P16 shows a lower evaporation

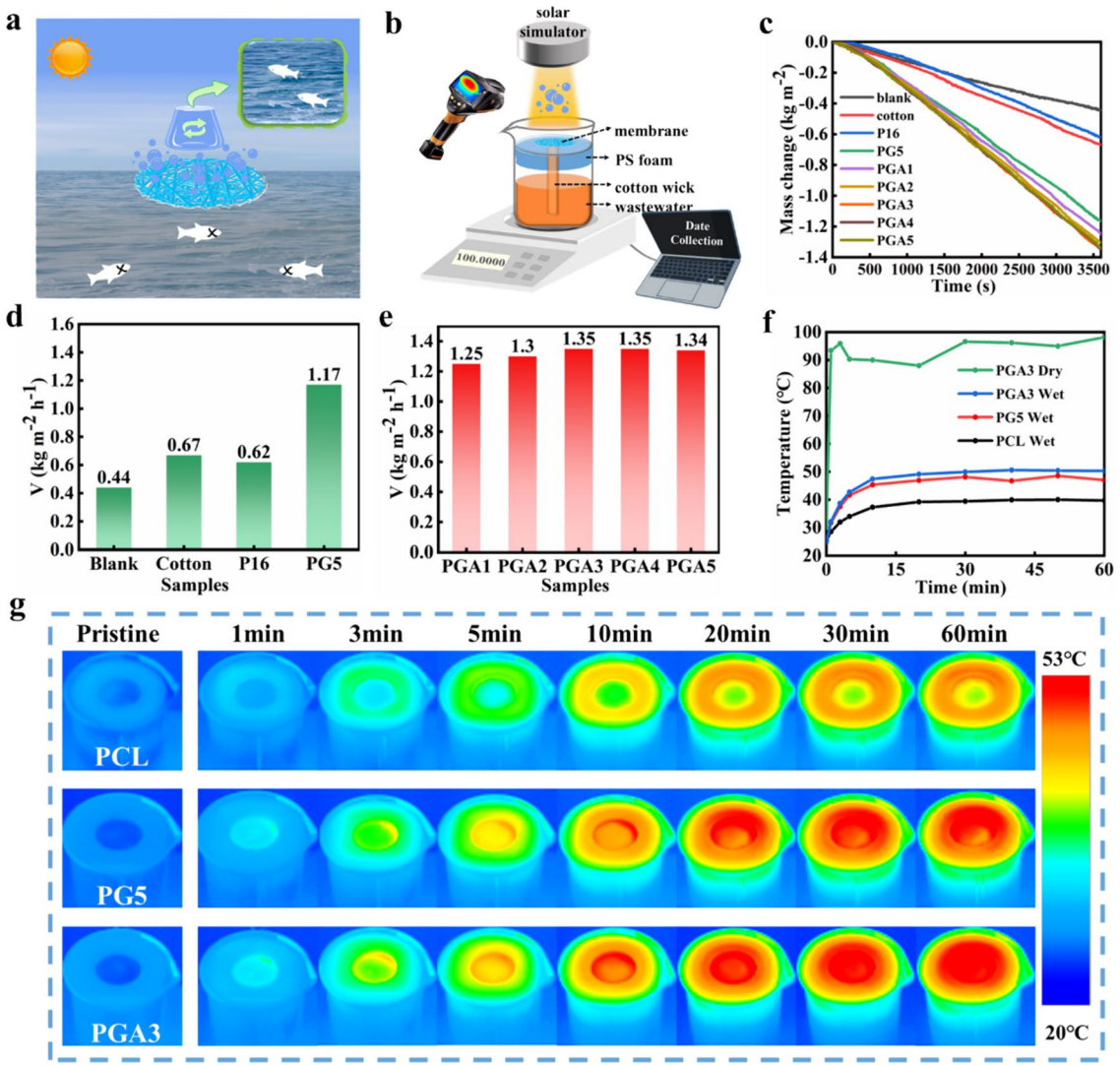

Fig. 4 **a** Schematic illustration of wastewater recycling by solar-driven evaporation. **b** Self-assemble lab scale evaporation evaluation system. **c** Curves of mass change over 1 h of irradiation. **d**, **e** Average evaporation rate of membranes over 1 h of irradiation. **f** Temperature–time relationship of membranes. **g** Infrared images of membranes at various time

rate of 0.62 kg m^{-2} h^{-1} because PCL is not photothermal material and the membrane is hydrophobic which hinders the transportation of water. On the contrary, although PG5 is also hydrophobic, the efficient photothermal material GO shows better solar absorption property which can still lead to a higher evaporation rate at 1.17 kg m^{-2} h^{-1}. Correspondingly, PGA membranes are all over 1.2 kg m^{-2} h^{-1} (PGA1 to PGA5 at 1.25, 1.30, 1.35, 1.35, and 1.34, respectively) owing to the synergistic effect of two photothermal materials GO/PANI and the super-hydrophilic surface of PGA, as shown in Fig. 4e.

On the other hand, the photothermal effect can be accessed by monitoring temperature rise under light intensity of 1 sun (1 kW m^{-2}). As shown in Fig. 4f, g, the surface temperature of pure PCL membrane reaches 39.7 °C after 1 h of irradiation, while that of PG5 increases to 47.0 °C, and PGA3 reaches around 50.3 °C. After illuminated for 30 min, the temperature of membrane surface generally gets stable, indicating the balance between heat generation and steam evaporation. The temperature variety is in accordance with the absorption result: the P16 absorbs the least solar energy which caused smallest temperature rise, while PGA3 absorbs the most solar energy, which leads to the largest temperature rise. Besides, the temperature in the wet state (evaporating DI water) is lower than in the dry state (without DI water), due to the cooling effect of DI water and the consumption of thermal energy to vaporize the water.

GO has wide-spectrum absorption capacity as a typical carbon material, while narrow bandgap material PANI can

be excited by low-energy photons due to protic acid doping since the photogenerated electrons can transfer between valence band (VB) and conduction band (CB), which promotes the thermal energy generated from accelerating electron transfer [64]. The synergistic effect between GO and PANI significantly enhances the light absorption capacity and the photothermal conversion capacity.

Although more PANI doping increases the evaporation property, it shows a limitation at PGA3, which may due to the fully occupation of polymerization sites and block of water transportation channel inside nanofibrous membrane. Therefore, PGA3 was adopted for further application. Natural seawater achieved from North Pacific Ocean (35.5774164, 139.7850123 in Toyoko Bay, Japan,) was used to evaluate the potential practical evaporation property. The mass change for 12 h constant irradiation and the evaporation rate every 0.5 h under 1 sun were recorded and calculated (Fig. 5a, b). Similar to DI water, the evaporation rate is gradually increased during the first 0.5 h, and does not change too much in the remaining 11.5 h. The highest evaporation rate is 1.38 kg m^{-2} h^{-1} during balance state. The evaporated vapor was collected and the concentrations of four main salt ions (Na^+, Mg^{2+}, K^+, and Ca^{2+}) were analyzed by an inductively coupled plasma emission spectroscopic analyzer (ICP). As shown in Fig. 5c, the concentrations of four ions are tremendously diminished by three to four orders of magnitude after evaporation, and they are obviously below the safe salinity line of World Health Organization (WHO) and Environmental Protection Agency (EPA) for drinking water standard.

Despite from seawater, textile dying water with toxic dyes and high salinity also causes great problem to ecosystem since everyone in the world demands for colorful clothes. Although most of the textile dyeing water is purified before

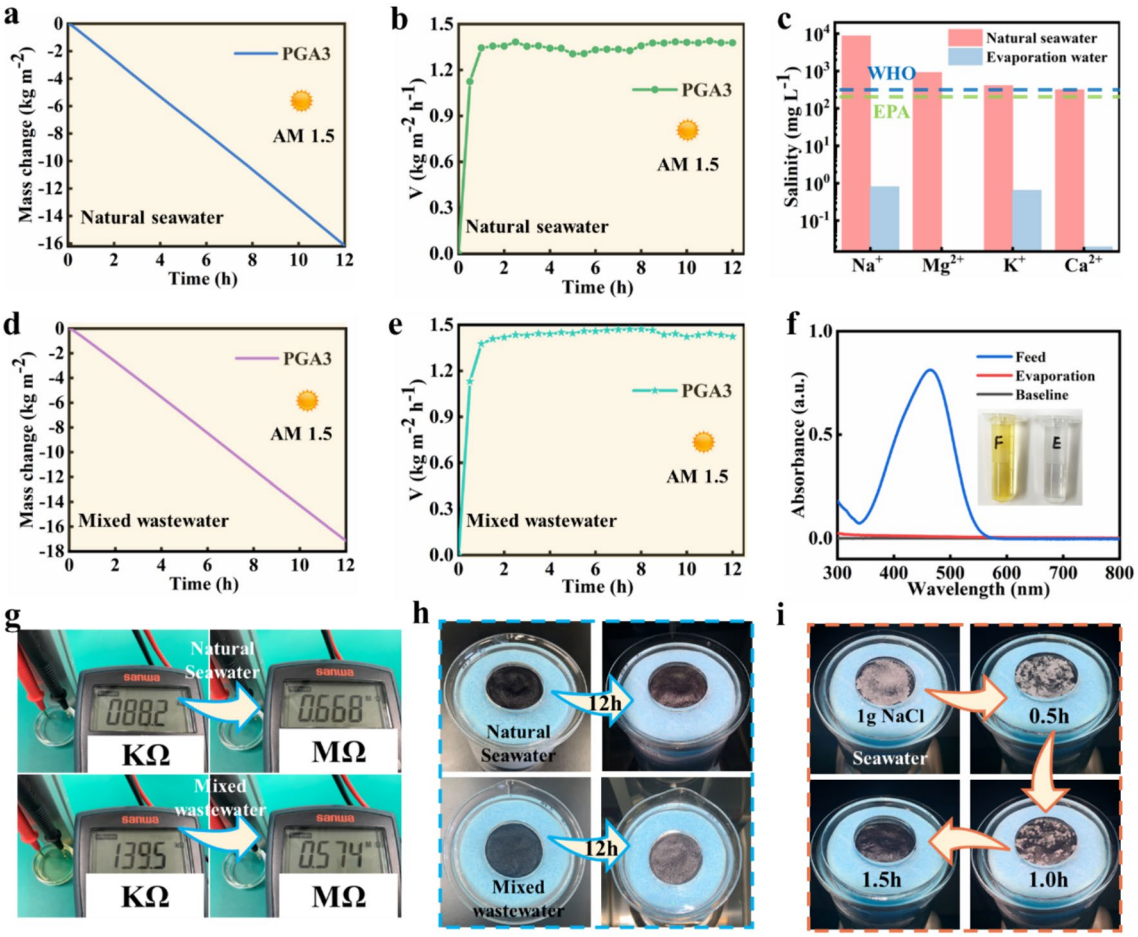

Fig. 5 The mass change **a** and evaporation rate **b** every 0.5 h of natural seawater under 12 h constant irradiation. **c** Concentrations of four main salt ions (Na^+, Mg^{2+}, K^+, and Ca^{2+}) before and after evaporation. The mass change **d** and evaporation rate **e** every 0.5 h of mixed wastewater under 12 h constant irradiation. **f** The UV absorbance spectra of feed and evaporated solution. **g** Conductivity of seawater before and after evaporation, mixed wastewater before and after evaporation, using a multimeter with a constant distance between electrodes and solution. **h** Surface images of membranes before and after 12 h evaporation. **i** Salt crystal dissolution phenomenon of PGA3 membrane

emission, part of it will still exists and eventually goes to lakes or the sea. Therefore, a mixed wastewater composed of 10,000 ppm NaCl and 10 ppm methyl orange (MO) was simulated and the evaporation performance was evaluated the same as seawater. The mass change and the evaporation rate trend are similar with seawater, and the highest evaporation rate of mix wastewater attains 1.47 kg m^{-2} h^{-1}, which exhibits good evaporation performance compared with other 2-dimensional membranes (Fig. 5d, e, Table S1). Moreover, the evaporation water of mixed wastewater was collected to assess dye purification effect. The UV–vis spectroscopy shows the decrease of absorbance compared to feed solution, which is close to baseline and demonstrates a high rejection of organic dyes, and the inset images also prove the clean quality of evaporation (Fig. 5f). Besides, the conductivity of seawater and mixed wastewater after evaporation is all lower than before and close to DI water attributed to the high rejection of salty and heavy metal ions (Figs. 5g and S4). Of note, even after 12 h constant service, no salt or dye crystal precipitates on the surface of membrane, which proves the high anti-fouling performance of prepared composite membrane (Fig. 5h). In order to verify this phenomenon, 1 g NaCl was put on the upper surface of a membrane which already worked for 12 h of seawater evaporation. It is noteworthy that all the salt crystals are dissolved after irradiated under 1 sun for 1.5 h (Fig. 5i). The remarkable salt/dye tolerance is owing to the super-hydrophilic surface and porous interconnect structure of the nanofibrous PGA membrane, which promote the infiltration-transportation of water molecules and dissolve of salt/dye ions [44, 46].

3.3 Photocatalytic Adsorption–Degradation Performance

In addition to photothermal evaporation, the photocatalytic adsorption–degradation can also make use of solar energy for sewage purification without any extra wastewater transportation or clean water collection equipment. Here, photocatalytic degradation and adsorption performance were assessed by organic dyes. Before evaluation, the

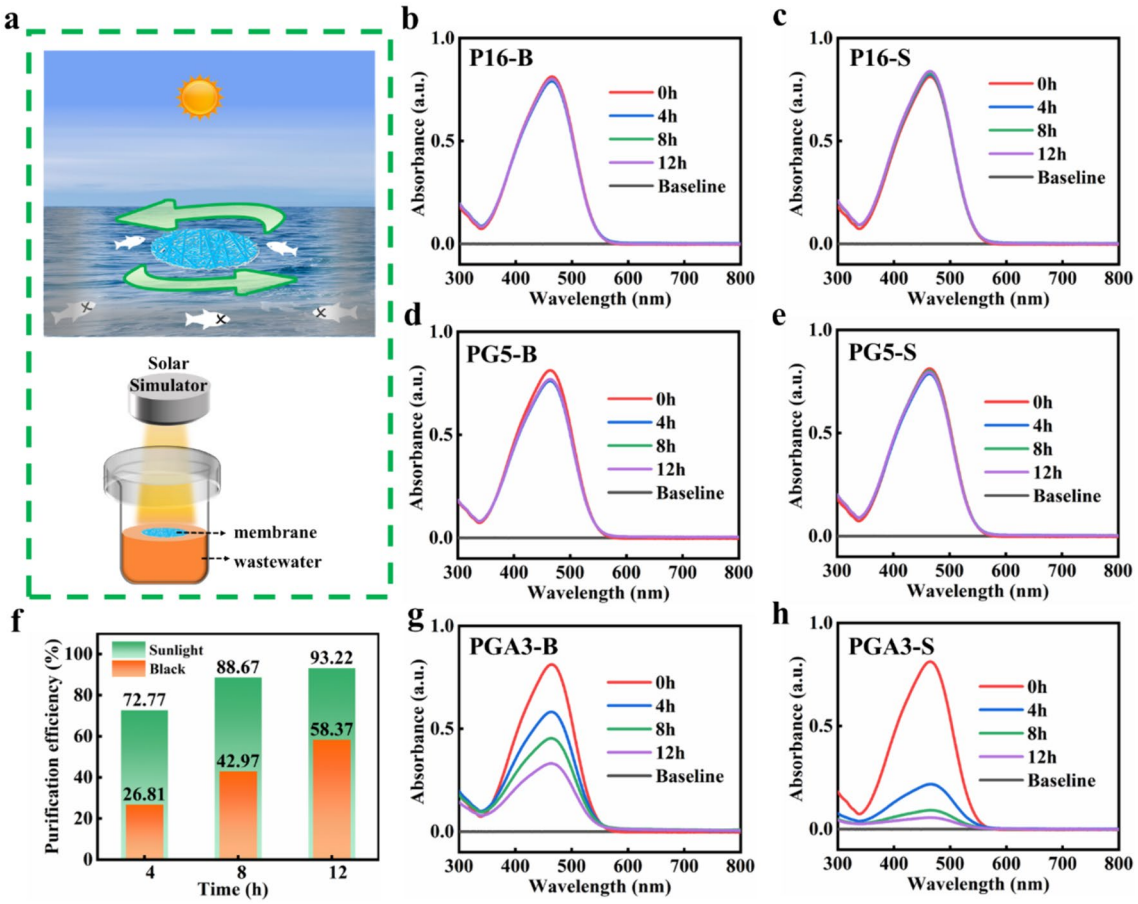

Fig. 6 **a** Schematic illustration of wastewater recycling by photocatalytic adsorption–degradation and self-assemble lab scale evaluation system. **b–h** UV absorbance spectra of P16, PG5, PGA3 in darkness (**b**, **d**, **g**) and under irradiation of 1 sun (**c**, **e**, **h**), respectively. **f** Purification efficiency of PGA3 in black and sunshine irradiation state

photostability of dyes was investigated to avoid the influence of dyes themselves. Three typical dye solutions of neutral red (NR), methyl orange (MO), and methylene blue (MEB) were irradiated under 1 sun for 12 h without membranes. Only MO still retains the original color while NR and MEB were both partly degraded (Fig. S6). Therefore, MO of 10 ppm is adopted as the simulating organic contaminant and the photocatalytic adsorption–degradation of three typical membranes was analyzed in sealed beakers (Figs. 6a and S7). The solution volume was fixed at 20 mL, and 3.5 mL of the solution was taken for the UV–vis spectroscopy test after every 4 h irradiation.

Two different environments were created for comparison, one is under irradiation of 1 sun (S) and another is in black (B) as control. For pure PCL membrane (P16), the absorbances almost retain the same even with the increase in irradiation time and in different circumstances, owing to the hydrophobic surface and no functional particle addition (Fig. 6b, c). The color changes of wastewater at different time point are in accordance with absorbance variety (Fig. S8). The absorbance of PG5 in black decreases slightly due to the absorption property originated from high specific area and oxygen-containing functional groups of GO (Fig. 6d). However, the mass ratio and the targeted functional groups of GO are not enough for PG5 to have a hydrophilic surface which hinders further diffusion of solution molecules. Besides, due to the photothermal effect of GO, when it is in irradiation state, a little part of water was evaporated to the top and side of the sealed beaker, which increased the concentration of MO, and thus the absorbance was higher than black situation (Fig. 6e).

Nevertheless, the absorbance of PGA3 in black decreases obviously proportion to processing time since PANI molecules contain plenty of primary and secondary amino and imine groups, which results in strong affinity with hydrophilic reactants, such as heavy metal ions and salt ions in water (Fig. 6g). As one of the most practical chelating functional groups, amino groups is beneficial to the enrichment of various pollutants from sewages owing to its high nucleophilicity and reactivity [65]. Of note, the concentration of MO in irradiation state diminishes even much more than black state (Fig. 6h). In order to quantitative compare the purification level of those two states, the concentration of MO mixture at maximum absorption wavelength was chosen for linear fitting, and therefore the linear correlation formula between the concentration of dye and the UV absorbance is established (Fig. S9). The purification efficiency of black state is 26.81% while the irradiation state reaches up to 72.77% after 4 h and attains 93.22% after 12 h, which verifies the superior photocatalytic adsorption–degradation performance (Fig. 6f). Accordingly, the adsorption capacity of the PGA3 in black at different time is shown in Fig. S10. As a special organic semiconductor photocatalysts, PANI consisting of benzenoid and quinonoid units has a wide range of delocalized π–π conjugated structure in molecules that can efficiently improve a rapid photoinduced charge separation and a relatively slow charge recombination [37, 38]. Furthermore, the PGA3 composite membrane is tested for three cycles without cleaning; the results are shown in Fig. S11. Compared to the first cycle, the purification effect decreases due to the excessive accumulation of dyes in the membrane. However, by increasing the irradiation time in the third cycle, it can still maintain the photocatalytic adsorption–degradation process. Therefore, it can be a useful supplement to solar-driven evaporation mode. The synergistic effect of GO and PANI contributes to excellent photocatalytic adsorption–degradation performance of the composite membrane and can also provide anti-fouling and photocatalytic self-cleaning property when used in solar-driven evaporation mode for complex wastewater that contains degradable organic contaminants.

3.4 Cross-Flow Filtration Performance

During rainy, cloudy, night, and other dark circumstance, solar will be invalid and other purification methods will be demanded as supplements. Thereby, traditional electric-driven filtration performance was evaluated by a custom-made cross-flow filtration device (Fig. 7a). The pure water flux J_0 was measured by filtrating 1 h of DI water at 1 bar after pre-pressed. Then it was switched to 10 ppm MO solutions for 1 h at 1 bar, so that the foulant flux J_1 and rejection ratio R can be measured. The flux of the membrane was calculated by the volume of permeate per unit time according to Eq. (2) and foulant rejection ratio R was estimated by Eq. (3).

$$J = \frac{\Delta V}{A \times \Delta t \times \Delta p} \tag{2}$$

$$R = \frac{C_1 - C_2}{C_1} \tag{3}$$

where J (L m^{-2} h^{-1} bar^{-1}) refers to flux, ΔV (L) refers to permeate volume, A (m^2) refers to effective membrane area, Δt (h) refers to collection time, Δp refers to transmembrane pressure (bar), C_1 and C_2 refer to concentrations of feed and permeate solutions, respectively.

In order to withstand the impact of water crash during cross-flow filtration and be able to filtrate small size foulants, two PGA3 membranes were hot-pressed into one piece at 45 °C for 10 min under 15 MPa pressure. Besides, P16 and PG5 were processed by same way, which were used as control. For the pure water flux J_0, membrane PGA3 shows the highest value at 46.75 L m^{-2} h^{-1} bar^{-1} (Fig. S12). The foulant flux J_1 of PGA3 decreases a bit

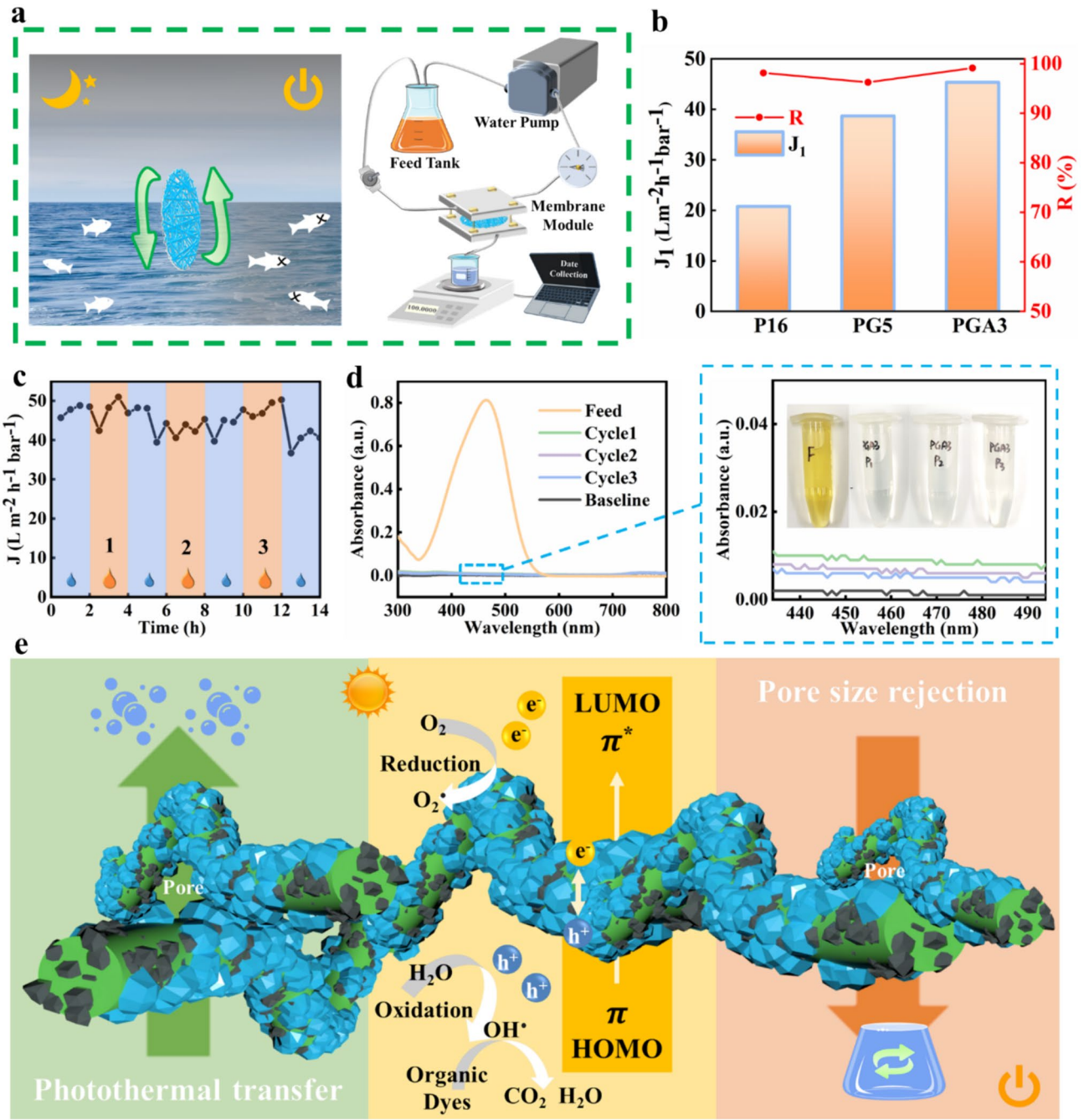

Fig. 7 **a** Schematic illustration of wastewater recycling by cross-flow filtration and self-assemble lab scale evaluation system. **b** Foulant flux and rejection of membranes. **c** Flux of every 0.5 h for the 2 h DI water and MO alternately lasted for 14 h constant filtration test. **d** UV absorbance spectra of permeate solution of three cycles MO filtration, inset picture is the corresponding images of feed and permeate solution. **e** Mechanism of trimode wastewater recycling

to 45.35 L m^{-2} h^{-1} bar^{-1} when filtrating 10 ppm MO sewage (P16 at 20.76 L m^{-2} h^{-1} bar^{-1} and PG3 at 38.69 L m^{-2} h^{-1} bar^{-1}, respectively) but achieves a high rejection of 99.15%, which is much better than P16 and PG5, owing to the superior hydrophilicity, structure stability, and adsorption property of membrane after PANI decoration (Fig. 7b). The PGA3 membrane exhibits excellent filtration performance compared with other 2-dimentional membranes (Table S2). Moreover, 14 h (2 h DI water, 2 h MO solution alternately) constant filtration test without cleaning was processed to verify the excellent separation performance of PGA3. The flux of every 0.5 h is calculated and although there is some fluctuation it stabilizes at 40.60 L m^{-2} h^{-1} bar^{-1} in the last 0.5 h, which is 89%

of the first 0.5 h (Fig. 7c). The UV absorption spectra of permeate solution (P1, P2, P3) for three MO cycles decrease sharply after cross-flow filtration (Fig. 7d), and the rejection rates are all over 99%, which indicates the effective filtration of organic dye foulants of fabricated membranes for long-term service.

3.5 Mechanism of the Eco-friendly Trimode Purification Membrane

The biodegradable polymer PCL serves as a basic framework for adding functional particles, thereby imposing a lighter burden on the environment (Fig. 7e). For the solar-driven evaporation mode, the combination of two photothermal materials, GO and PANI, greatly increases the absorption of solar energy in the whole UV–vis–NIR spectra. Furthermore, light is continuously reflected within the pores and nanofibers of the electrospinning membrane, optimizing diffuse reflection and enhancing light absorption. Thus, the composite membrane can effectively transfer solar energy to thermal energy and then heat the water solution into vapor through the membrane, which can be harvested as clean water since the boiling point of contaminants is quite higher than water. Besides, the super-hydrophilic nature of membrane allows it to disperse salt and dye ions promptly, preventing crystallization, thereby enhancing the service efficiency and life cycle.

For the photocatalytic adsorption–degradation mode, (1) first, the super-hydrophilic surface allows solution to fully penetrate into membrane. (2) Furthermore, the high specific surface area of GO and PANI particles, along with the affinity of amino groups in PANI, enhances the adsorption of contaminants on the membrane surface. (3) After that, the efficient solar absorption provides photons with energy the same as or higher than the band gap energy of the semiconductor polymer PANI, so that some electrons in the valence band (VB of the highest occupied molecular orbital, HOMO) may be excited to the conduction band (CB of the lowest unoccupied molecular orbital, LUMO). Therefore, plenty of negatively charged electrons (e^-) appear in CB while positively charged holes (h^+) stay in VB, which triggers chemical transformation of reduction and oxidation, and the organic dye can eventually be oxidized and degraded into CO_2 and H_2O.

For the cross-flow filtration performance, on the one hand, the interconnect structure of nanofibrous membrane and PANI decoration provides lots of small pores, which can intercept contaminants of large size, but permit small water molecules to pass through. Besides, the super-hydrophilic surface of PGA membrane provides the possibility of forming a hydration layer between the membrane and solution, which can hold back foulants ions. On the other hand, some parts of foulants can be absorbed by the membrane due to the synergistic adsorption effect of GO/PANI particles and nanofibers, which can be rushed and flow back to feed tank by cross-flow filtration method.

4 Conclusions

In summary, an attempt has been made to establish a trimode composite membrane for solving water crisis problems. The biodegradable substrate PCL electrospinning nanofibrous membrane showed an eco-friendly option as a purification membrane. When nanoparticles of GO are blended in and then combined with PANI decoration, the composite membrane can be used in multiple scenarios. The composite membrane can work stably for 12 h constantly, both for natural seawater and mixed salt/dye wastewater; the highest evaporation rate can reach up to 1.47 kg m^{-2} h^{-1} and the water quality is better than drinking water (the concentration of four main salt ions are far below the drinking water standard of WHO and EPA). The membrane can also be used in photothermal adsorption–degradation mode, which improves the self-cleaning property and reduces equipment demand. Besides, the cross-flow filtration mode as a supplement can also effectively reject 99% organic dyes with a higher flux of over 40 L m^{-2} h^{-1} bar^{-1}. This facile trimode design shows a sustainable strategy for hybrid nanofibrous membranes with eco-friendly and energy-saving properties, which is promising for long-term service and multi-scenario application of wastewater recycling.

Supplementary Information The online version contains supplementary material available at https://doi.org/10.1007/s42765-024-00430-8.

Acknowledgements This work was supported by the JSPS KAKENHI (Grant No. JP20H00288).

Funding Open Access funding partially provided by Shinshu University.

Data availability The data that support the findings of this study are available from the corresponding author upon reasonable request.

Declarations

Conflict of interest The authors declare that they have no conflict of interest.

References

1. Cremer PS, Flood AH, Gibb BC, Mobley DL. Collaborative routes to clarifying the murky waters of aqueous supramolecular chemistry. *Nat Chem*. **2018**;*10*:8.
2. Sladen A, Rivet D, Ampuero JP, Barros LD, Hello Y, Calbris G, Lamare P. Distributed sensing of earthquakes and ocean-solid Earth interactions on seafloor telecom cables. *Nat Commun*. **2019**;*10*:5777.
3. Kocher JD, Menon AK. Addressing global water stress using desalination and atmospheric water harvesting: a thermodynamic and technoeconomic perspective. *Energy Environ Sci*. **2023**;*16*:4983.
4. Kim N, Elbert J, Kim C, Su X. Redox-copolymers for nanofiltration-enabled electrodialysis. *ACS Energy Lett*. **2023**;*8*:2097.
5. Jennifer Ross. The sustainable development goals report. 1rd ed. United Nation publications, **2023**.
6. Lin Z, Cao N, Li C, Sun R, Li W, Chen L, Sun Y, Zhang H, Pang J, Jiang Z. Micro-nanostructure tuning of PEEK porous membrane surface based on PANI in-situ growth for antifouling ultrafiltration membranes. *J Membrane Sci*. **2022**;*663*:121058.
7. Ye Z, Zhang Y, Hou L, Zhang M, Zhu Y, Yang Y. Preparation of a GO/PB-modified nanofiltration membrane for removal of radioactive cesium and strontium from water. *Chem Eng J*. **2022**;*446*:137143.
8. Zheng J, Zhao R, Uliana AA, Liu Y, Donnea DD, Zhang X, Xu D, Gao Q, Jin P, Liu Y, Volodine A, Zhu J, Bruggen BV. Separation of textile wastewater using a highly permeable resveratrol-based loose nanofiltration membrane with excellent anti-fouling performance. *Chem Eng J*. **2022**;*434*:134705.
9. Yan XY, Wang Q, Wang Y, Fu ZJ, Wang ZY, Mamba B, Sun SP. Designing durable self-cleaning nanofiltration membranes via sol–gel assisted interfacial polymerization for textile wastewater treatment. *Sep Purif Technol*. **2022**;*289*:120752.
10. Sankar SN, Fernandes J, dos Santos MB, Espiña B, Alpuim P, Díez AG, Lanceros MS, Saini L, Kaushik S, Kalon G, Capasso A. Stable graphene membranes for selective ion transport and emerging contaminants removal in water. *Adv Funct Mater*. **2023**;*33*:2214889.
11. Chen X, Li Y, Xu L, Zhang D, Guan Y, Dong L, Bao M, Wang Z. Thermosensitive microfibril cellulose/MnO_2 membrane: dual network structure, photothermal smart modulation for switchable emulsion separation. *ACS Sustain Chem Eng*. **2023**;*11*:931.
12. Cheng X, Li T, Yan L, Jiao Y, Zhang Y, Wang K, Cheng Z, Ma J, Shao L. Biodegradable electrospinning superhydrophilic nanofiber membranes for ultrafast oil–water separation. *Sci Adv*. **2023**;9:eadh8195.
13. Ren G, Wan K, Kong H, Guo L, Wang Y, Liu X, Wei G. Recent advance in biomass membranes: fabrication, functional regulation, and antimicrobial applications. *Carbohyd Polym*. **2023**;*305*:120537.
14. Qin Y, Shen H, Han L, Zhu Z, Pan F, Yang S, Yin X. Mechanically robust Janus poly(lactic acid) hybrid fibrous membranes toward highly efficient switchable separation of surfactant-stabilized oil/water emulsions. *ACS Appl Mater Interfaces*. **2020**;*12*:50879.
15. Deng S, Liu X, Liao J, Lin H, Liu F. PEI modified multi-walled carbon nanotube as a novel additive in PAN nanofiber membrane for enhanced removal of heavy metal ions. *Chem Eng J*. **2019**;*375*:122086.
16. Wang K, He H, Zhang TC, Liang Y, Yuan S. Self-locked and self-cleaning membranes for efficient removal of insoluble and soluble organic pollutants from water. *ACS Appl Mater Interfaces*. **2021**;*13*:6906.
17. Zhu Z, Liu Y, Hou H, Shi W, Qu F, Cui F, Wang W. Dual-bioinspired design for constructing membranes with super hydrophobicity for direct contact membrane distillation. *Environ Sci Technol*. **2018**;*52*:3027.
18. Ali J, Alhseinat E, Jaoude MA, Nashef IMA, Adeyemi IA, Aminabhavi TM, Arafat HA. A mixed matrix polyimide ultrafiltration membrane for efficient removal of Bentazon from water. *Chem Eng J*. **2022**;*433*:134596.
19. Wu S, Li K, Shi W, Cai J. Chitosan/polyvinylpyrrolidone/polyvinyl alcohol/carbon nanotubes dual layers nanofibrous membrane constructed by electrospinning-electrospray for water purification. *Carbohyd Polym*. **2022**;*294*:119756.
20. Woodruff MA, Hutmacher DW. The return of a forgotten polymer—polycaprolactone in the 21st century. *Prog in Polym Sci*. **2010**;*35*:1217.
21. Labet M, Thielemans W. Synthesis of polycaprolactone: a review. *Chem Soc Rev*. **2016**;*38*:3484.
22. Han B, Zhang YL, Chen QD, Sun HB. Carbon-based photothermal actuators. *Adv Funct Mater*. **2018**;*28*:1802235.
23. Fan X, Ding Y, Liu Y, Liang J, Chen Y. Plasmonic $Ti_3C_2T_x$ MXene enables highly efficient photothermal conversion for healable and transparent wearable device. *ACS Nano*. **2019**;*13*:8124.
24. Zhang R, Han W, Jiang H, Wang X, Wang B, Liu C, Shen C. PBAT/MXene monolithic solar vapor generator with high efficiency on seawater evaporation and swage purification. *Desalination*. **2022**;*541*:116015.
25. Yu Y, Wu H, Yu Y, Shi J, Morikawa H, Zhu C. Energy saving dual-mode recycling of wastewater by MWCNTs-COOK/PDA/PVA assisted composite membrane. *Chem Eng J*. **2023**;*475*:146202.
26. Zhao J, Liu Z, Low SC, Xu Z, Tan SH. Electrospinning technique meets solar energy: electrospun nanofiber-based evaporation systems for solar steam generation. *Adv Fiber Mater*. **2023**;*5*:1318.
27. Wu W, Xu Y, Ma X, Tian Z, Zhang C, Han J, Han X, He S, Duan G, Li Y. Cellulose-based interfacial solar evaporators: structural regulation and performance manipulation. *Adv Funct Mater*. **2023**;*33*:2302351.
28. Li Z, Zhang X, Liu J, Shi R, Waterhouse GIN, Wen XD, Zhang T. Titania-supported Ni_2P/Ni catalysts for selective solar-driven CO hydrogenation. *Adv Mater*. **2021**;*33*:2103248.
29. Li Y, Gao T, Yang Z, Chen C, Luo W, Song J, Hitz E, Jia C, Zhou Y, Liu B, Yang B, Hu L. 3D-printed, all-in-one evaporator for high-efficiency solar steam generation under 1 sun illumination. *Adv Mater*. **2017**;*29*:1700981.
30. Zhang X, Sun Y, Ju S, Ye J, Hu X, Chen W, Yao L, Xia G, Fang F, Sun D, Yu X. Solar-driven reversible hydrogen storage. *Adv Mater*. **2023**;*35*:2206946.
31. Qiu J, Shi Y, Xia Y. Polydopamine nano bottles with photothermal capability for controlled release and related applications. *Adv Mater*. **2021**;*33*:2104729.
32. Zha Z, Yue X, Ren Q, Dai Z. Uniform polypyrrole nanoparticles with high photothermal conversion efficiency for photothermal ablation of cancer cells. *Adv Mater*. **2013**;*25*:777.
33. Zeng W, Wu X, Chen T, Sun S, Shi Z, Liu J, Ji X, Zeng X, Guan J, Mei L, Wu M. Renal-clearable ultrasmall polypyrrole nanoparticles with size-regulated property for second near-infrared light-mediated photothermal therapy. *Adv Funct Mater*. **2021**;*31*:2008362.

34. Wu J, Zhang Y, Jiang K, Wang X, Blum NT, Zhang J, Jiang S, Lin J, Huang P. Enzyme-engineered conjugated polymer nanoplatform for activatable companion diagnostics and multistage augmented synergistic therapy. *Adv Mater*. **2022**;*34*:2200062.
35. Lin Y, Wu S, Yang C, Chen M, Li X. Preparation of size-controlled silver phosphate catalysts and their enhanced photocatalysis performance via synergetic effect with MWCNTs and PANI. *Appl Catal B Environ Energy*. **2019**;*245*:71.
36. Yang YX, Wang DY, Liao WX, Zeng HY, Wu YJ, Li LX, Feng W, Xue J, Cao HB, Chen JQ, Huang YY, Zheng YY, Wang P, Liu J, Guo MC, Zhou H, Fan X. Arch-bridge photothermal fabric with efficient warp-direction water paths for continuous solar desalination. *Adv Fiber Mater*. **2024**. https://doi.org/10.1007/s42765-024-00392-x.
37. Xiao Y, Jiang Y, Zhou E, Zhang W, Liu Y, Zhang J, Wu X, Qi Q, Liu Z. In-suit fabricating an efficient electronic transport channels via S-scheme polyaniline/$Cd_{0.5}Zn_{0.5}S$ heterojunction for rapid removal of tetracycline hydrochloride and hydrogen production. *J Mater Sci Technol*. **2023**; *153*: 205.
38. Kausor MA, Chakrabortty D. Polyaniline (PANI) grafted hierarchical heterostructure nanocomposites for photocatalytic degradation of organic pollutants in waste water: a review. *Surf Interfaces*. **2022**;*31*:102079.
39. Xu W, Lim TS, Seo HK, Min SY, Cho H, Park MH, Kim YH, Lee TW. N-doped graphene field-effect transistors with enhanced electron mobility and air-stability. *Small*. **2014**;*10*:1999.
40. Lee C, Wei X, Kysar JW, Hone J. Measurement of the elastic properties and intrinsic strength of monolayer graphene. *Science*. **2008**;*321*:385.
41. Xin G, Sun H, Hu T, Fard HR, Sun X, Koratkar N, Borca TT, Lian J. Large-area freestanding graphene paper for superior thermal management. *Adv Mater*. **2014**;*26*:4521.
42. Chen Q, Zhong Y, Zhang Z, Zhao X, Huang M, Zhen Z, He Y, Zhu H. Long-term electrical conductivity stability of graphene under uncontrolled ambient conditions. *Carbon*. **2018**;*133*:410.
43. Safaei A, Chandra S, Leuenberger MN, Chanda D. Wide angle dynamically tunable enhanced infrared absorption on large-area nanopatterned graphene. *ACS Nano*. **2018**;*13*:421.
44. Kong Y, Dan H, Kong W, Gao Y, Shang Y, Ji K, Yue Q, Gao B. Self-floating maize straw/graphene aerogel synthesis based on microbubble and ice crystal templates for efficient solar-driven interfacial water evaporation. *J Mater Chem A*. **2020**;*8*:24734.
45. Lin H, Sturmberg BCP, Lin KT, Yang Y, Zheng X, Chong TK, Sterke CM, Jia B. A 90-nm-thick graphene metamaterial for strong and extremely broadband absorption of unpolarized light. *Nat Photonics*. **2019**;*13*:270.
46. Xu J, Xu F, Qian M, Li Z, Sun P, Hong Z, Huang F. Copper nanodot-embedded graphene urchins of nearly full-spectrum solar absorption and extraordinary solar desalination. *Nano Energy*. **2018**;*53*:425.
47. Yang HC, Lu F, Li HN, Zhang C, Darling SB, Xu ZK. Membranes in solar-driven evaporation: design principles and applications. *Adv Funct Mater*. **2023**;*33*:2304580.
48. Osswald S, Flahaut E, Ye H, Gogotsi Y. Elimination of D-band in Raman spectra of double-wall carbon nanotubes by oxidation. *Chem Phys Lett*. **2005**;*402*:422.
49. Narute P, Sharbidre RS, Lee CJ, Park BC, Jung HJ, Kim JH, Hong SG. Structural integrity preserving and residue-free transfer of large-area wrinkled graphene onto polymeric substrates. *ACS Nano*. **2022**;*16*:9871.
50. Anjum H, Johari K, Appusamy A, Gnanasundaram N, Thanabalan M. Surface modification and characterization of carbonaceous adsorbents for the efficient removal of oil pollutants. *J Hazard Mater*. **2019**;*379*:120673.
51. Wepasnick KA, Smith BA, Schrote KE, Wilson HK, Diegelmann SR, Fairbrother DH. Surface and structural characterization of multi-walled carbon nanotubes following different oxidative treatments. *Carbon*. **2011**;*49*:24.
52. Hussain Z, Ullah S, Yan J, Wang Z, Ullah I, Ahmad Z, Zhang Y, Cao Y, Wang L, Mansoorianfar M, Pei R. Electrospun tannin-rich nanofibrous solid-state membrane for wastewater environmental monitoring and remediation. *Chemosphere*. **2022**;*307*:135810.
53. Feng JX, Tong SY, Tong YX, Li GR. Pt-like hydrogen evolution electrocatalysis on PANI/CoP hybrid nanowires by weakening the shackles of hydrogen ions on the surfaces of catalysts. *J Am Chem Soc*. **2018**;*140*:5118.
54. Lin Z, Cao N, Li C, Sun R, Li W, Chen L, Sun Y, Zhang H, Pang J, Jiang Z. Micro-nanostructure tuning of PEEK porous membrane surface based on PANI in-situ growth for antifouling ultrafiltration membranes. *J Membr Sci*. **2022**;*663*:121058.
55. Lan X, Wang H, Liu Y, Chen X, Xiong J, Mai R, Wang Y, Cai N, Chen X, Tang Y. Biodegradable trilayered micro/nano-fibrous membranes with efficient filtration, directional moisture transport and antibacterial properties. *Chem Eng J*. **2022**;*447*:137518.
56. Pagno V, Módenes AN, Dragunski DC, Fiorentin LD, Caetano J, Guellis C, Gonçalves BC, Anjos EV, Pagno F, Martinelli V. Heat treatment of polymeric PBAT/PCL membranes containing activated carbon from Brazil nutshell biomass obtained by electrospinning and applied in drug removal. *J Environ Chem Eng*. **2020**;*8*:104159.
57. Scaffaro R, Gammino M, Maio A. Wet electrospinning-aided self-assembly of multifunctional GO-CNT@PCL core-shell nanocomposites with spider leg bioinspired hierarchical architectures. *Compos Sci Technol*. **2022**;*221*:109363.
58. Wu C, Zhou T, Du Y, Dou S, Zhang H, Jiang L, Cheng Q. Strong bioinspired HPA-rGO nanocomposite films via interfacial interactions for flexible supercapacitors. *Nano Energy*. **2019**;*58*:517.
59. Zhao Y, Tang GS, Yu ZZ, Qi JS. The effect of graphite oxide on the thermoelectric properties of polyaniline. *Carbon*. **2012**;*50*:3064.
60. Xu D, Zhu Z, Li J. Recent progress in electrospun nanofibers for the membrane distillation of hypersaline wastewaters. *Adv Fiber Mater*. **2022**;*4*:1357.
61. Han J, Xing WQ, Yan J, Wen J, Liu YT, Wang YQ, Wu ZF, Tang LC, Gao JF. Stretchable and super hydrophilic polyaniline/halloysite decorated nanofiber composite evaporator for high efficiency seawater desalination. *Adv Fiber Mater*. **2022**;*4*:1233.
62. Liu CY, Gui JX, Li DH, Liu ZX, Shen YJ, Huang W, Wang HH, Tian XL. Ionic power generation on a scalable cellulose @ polypyrrole membrane: the role of water and thermal gradients. *Adv Fiber Mater*. **2024**;*6*:243.
63. Lu JQ, Bai T, Wang D, Yu HJ, Wang QX, Niu ZX, Hu Y, Liu XY, Han GP, Cheng WL. Electrospun polyacrylonitrile membrane in situ modified with cellulose nanocrystal anchoring TiO_2 for oily wastewater recovery. *Adv Fiber Mater*. **2023**;*5*:2055.
64. Chen H, Pan G, Yan M, Wang F, Wu Y, Guo C. Janus membrane with enhanced interfacial activation for solar evaporation. *J Energy Chem*. **2023**;*87*:1.
65. Shao D, Hou G, Li J, Wen T, Ren X, Wang X. PANI/GO as a super adsorbent for the selective adsorption of uranium(VI). *Chem Eng J*. **2014**;*255*:604.